

EndNet: Sparse AutoEncoder Network for Endmember Extraction and Hyperspectral Unmixing

Savas Ozkan, *Member, IEEE*, Berk Kaya, Ersin Esen, *Member, IEEE*, and Gozde Bozdagi Akar, *Senior Member, IEEE*

Abstract—Data acquired from multi-channel sensors is a highly valuable asset to interpret the environment for a variety of remote sensing applications. However, low spatial resolution is a critical limitation for the sensors and the constituent materials of a scene can be mixed in different fractions due to their spatial interactions. Spectral unmixing is a technique that allows us to obtain the material spectral signatures with their fractions from data. In this paper, we propose a novel hyperspectral unmixing scheme, called *EndNet*, that is based on a two-staged autoencoder network. This well-known structure is completely enhanced and restructured by introducing additional layers and a projection metric (i.e spectral angle distance (SAD) instead of inner product) to achieve an optimum solution. Moreover, we present a novel loss function that is composed of Kullback-Leibler divergence term with SAD similarity and additional penalty terms to improve the sparsity of the estimates. These modifications enable us to set the common properties of endmembers such as non-linearity and sparsity for autoencoder networks. Lastly, due to the stochastic-gradient based approach, the method is scalable for large-scale data and it can be accelerated on Graphical Processing Units (GPUs). To demonstrate the superiority of our method, we conduct extensive experiments on several well-known datasets. The obtained results confirm that our method considerably improves the performance compared to the state-of-the-art techniques in literature.

Index Terms—Hyperspectral Unmixing, Hyperspectral Unmixing, Endmember Extraction, Sparse Autoencoder.

I. INTRODUCTION

IN remote sensing, hyperspectral data is an essential imaging sensory output to gain an insight about the Earth by utilizing information beyond the human visible spectrum. This sensor type has been widely used in a variety of remote sensing applications from environmental monitoring to military surveillance for years [1]. However, spatial resolution of the sensors is very limited compared to other optics operating in visible spectrum domain. Inevitably, this scatters the material responses exhibited in data in which the resultant pixels can be concurrently exposed to several constituent materials. This raises a critical issue that the constituent materials signatures (endmembers) and their fractions (abundances maps) should be determined from data before taking any further step in hyperspectral applications.

To derive a simple solution for the problem, the mixture of constituent materials is generally formulated with a linear model [2] where each data point on an image $\mathbf{x} \in \mathbb{R}^D$ is a linear combination of endmembers $\mathbf{E} = [\mathbf{e}_1, \mathbf{e}_2, \dots, \mathbf{e}_K] \in \mathbb{R}^{D \times K}$ with different fractions $\mathbf{y} = [y_1, y_2, \dots, y_K] \in \mathbb{R}^K$. Here, K denotes the number of endmembers on an image. In addition, this formulation has an additional term η -it is assumed to be a zero mean Gaussian noise- to simulate possible noise sources in the process such as sensor readout noise or illumination variability due to surface topography:

$$\mathbf{x} = \sum_{k=1}^K \mathbf{e}_k y_k + \eta, \quad s.t. \quad y_k > 0, \quad \sum_{k=1}^K y_k = 1 \quad (1)$$

Moreover, unmixing of hyperspectral data is separated into two major steps (note that we assume that the optimum number of endmember is known) as endmember extraction and quantifying the abundances of these endmembers per pixel. These two unknown variables can be solved either simultaneously or individually depending on the approaches.

In literature, linear and nonlinear models have been vastly studied and several promising methods have been proposed as follows.

For linear model, geometrical volume-based algorithms are quite common to identify endmembers from hyperspectral data [3], [4], [5], [6]. Basically, they treat the distribution of data samples as a simplex set [4]. They ultimately embrace the fact that the vertices of this simplex set correspond to the endmembers since all of the data samples can be spanned with these points.

By exploiting this assumption (i.e. simplex set) and the notion of presence of pure pixels, the most straightforward linear solution is to determine unmixed pixels from data for all materials [6], [7]. Later, Vertex Component Analysis (VCA)-like methods [3], [5] extend the assumption by projecting and imposing an orthogonality condition onto endmembers in their estimation. However, these methods have severe drawbacks as pointed out in [8]. Briefly, the mixture of materials in both macroscopic and microscopic levels [8], [9] can lead to erroneous spectral estimates. Therefore, the pure-pixel assumption can collapse with the lack of the purities of one or more materials in data. To solve these drawbacks, several concepts are introduced in literature [10], [11], [12], [13], [14] that basically add a margin to the derivation with extra constraints or a kernel structure. Thus, this produces more reliable outputs even if the data does not directly satisfy the purest material condition. However, particularly for [13], [14], presence of

S. Ozkan is with the Image Processing Department, TUBITAK Space Technologies Research Institute and the Department of Electrical and Electronics Engineering, Middle East Technical University, Ankara, Turkey e-mail: savas.ozkan@tubitak.gov.tr

B. Kaya and G.B. Akar are with the Department of Electrical and Electronics Engineering, Middle East Technical University, Ankara, Turkey.

E. Esen is with the Image Processing Department, TUBITAK Space Technologies Research Institute, Ankara, Turkey

outlier and noise can significantly reduce the performance of the suboptimal solution of the methods as explained in [15].

Lastly, methods utilizing a codebook of endmembers (collected with a spectrometry and available in a spectral library) [8], [16] are another solution to identify abundance maps and corresponding endmembers from hyperspectral data. By regarding the similar observation throughout our paper, the importance of sparsity is particularly emphasized in these studies.

Although the linear mixture model is simple and provides practical advantages, it is not quite adequate to solve the problem. Multiple scattering effects [17], microscopic-level material mixtures [8], [9] and water-absorbed environments [18] can be shown as severe natural cases that cannot be handled by the linear models. One way to deal with such scenarios is to use unsupervised nonlinear projections of data [19], [20]. However, this type of approaches needs high memory requirement and computational workload, thus it eventually reduces the scalability of the methods for large-scale data. An alternative strategy is to replace the conventional operations with different kernel functions in derivation. This methodology simply introduces a distortion onto endmembers and abundance estimates to enhance the robustness against nonlinear interactions [21], [22], [23], [24], [25], [26], [27], [28].

Leveraging supervised data with neural-network architectures is another solution proposed for this problem [29], [30], [31], [32], [33]. Although critical discussions are presented for optimum training sample selection, the quality of training samples drastically influences the performance. Also, data labeling is costly and impractical compared to unsupervised approaches. Therefore, the estimation of endmembers and abundance maps should be blind.

In literature, neural network approaches have been applied to different hyperspectral applications as well. [34] presents a three-staged denoising model based on a conventional autoencoder structure for multi-channel data. In another study [35], the authors explain a sparse autoencoder which detects abnormal objects in the scene by assessing the deformation of material signatures from the backgrounds in the reconstruction step. However, these methods merely utilize the conventional architectures in their problems and do not make important contributions to hyperspectral domain.

Finally, very recent study [36] introduces a set of components to the encoder layer of an autoencoder that particularly helps to increase the sparsity of endmembers as well as abundance map estimates.

As mentioned, the adaptation of neural network structure to hyperspectral unmixing is not completely solved in literature, especially for unsupervised setup. To the best of our knowledge, our method will be the first successful attempt based on an autoencoder network that outperforms the conventional methods all in an unsupervised manner.

Our Contribution: In this study, we propose a novel two-staged neural network autoencoder and an end-to-end learning scheme that are specialized to extract endmembers with their pixel abundances from hyperspectral data. Our method uses some of the major observations previously introduced for

hyperspectral unmixing, however it significantly differs from the traditional autoencoder pipeline with novel features.

Similar to [13], [14], we observed that rather than strictly obeying all of the physical properties of the endmembers, solving the problem with some of the constraints can yield better results. More clearly, no constraint is imposed to set the value range of the estimated endmembers to $[0, 1]$ by the fact that spectral angle distance (SAD) is a critical objective in our loss function and it enforces to maximize angular similarity between samples rather than their perfect spectral match. However, the negative values of endmembers are penalized by SAD metric, thus, this constraint is automatically supplied in the learning process. But, other constraints such as sum-to-one constraint (i.e. $\sum_{k=1}^K y_k = 1$) and greater than zero constraint (i.e. $y_k > 0$) are preserved because of the internal characteristics of components in the architecture which will be explained in the following section.

In our method, first, sparsity and non-linearity are effectively applied by a rectified activation function, ReLU (i.e. bounds the negative responses of hidden abstracts) [37] and a normalization layer [38] as in [36]. This adaptation enables us to set bias terms to zero in the formulation and it eliminates the adverse effects of bias terms in the solution. However, the complete sparsity is still missing and it is prone to overfitting due to the fact that the network tends to generate hidden responses constantly for highly correlated materials. In other words, a small number of responses should contribute to the composition of a pixel for a practical solution. In our paper, this is achieved by hard-response selection and regularization techniques [39], [40] which allow only the highest responses of abundance estimates contribute to the reconstruction stage. To this end, it leads to better solution and improves the sparsity for endmembers as well as abundance estimates.

Second, we replace inner product operators at encoder layer with spectral angle distance (SAD) to obtain more discriminative hidden abstracts. Third, we introduce an extra set of penalty terms to the loss function in which they can enforce closer angular similarity between the original and the reconstructed data along with the standard Euclidean (l_2) reconstruction penalty. Also, sparse hidden abstracts are achieved with additional penalty terms. Fourth, on the contrary to some conventional unmixing approaches [3], [6], [24], [27], [28], our method solves the problem by optimizing endmembers and their corresponding abundances concurrently with a stochastic gradient-based solver. This leads to the optimum solutions for both endmembers and abundance maps while it scales the method for large-scale data.

Lastly, we observed that usage of VCA-like [3], [6], [27] methods as an autoencoder filter initializer helps us to attain state-of-the-art performance. This makes the filters converge faster to the global optimum. Note that this step is practiced previously in different optimization-based algorithms [14] and it similarly avoids the parameters stuck to poor quality solutions.

The remainder of our paper is organized as follows. First, necessary information about the proposed architecture and the optimization step are presented in details in Section 2. Section 3 is reserved for the results and discussions on the experiments

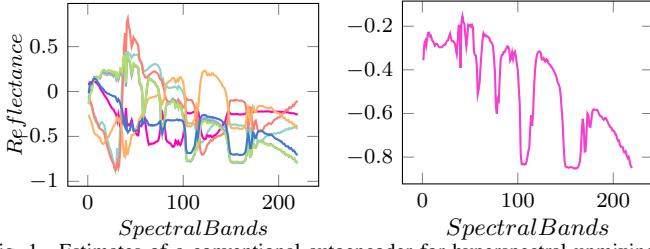


Fig. 1. Estimates of a conventional autoencoder for hyperspectral unmixing problem. First plot (left side) shows decoder layer parameters, $\mathbf{W}^{(e)}$, which intuitively correspond to endmembers while second plot (right side) illustrates bias term response. As can be seen from the results, bias term acts like one of the endmembers exhibited in the scene. Moreover, the estimated signatures (left side) do not satisfy the physical conditions of endmembers, i.e. $y_k > 0$.

conducted on several publicly available datasets. Conclusion and overall discussions are reported in Section 4.

II. SPECTRAL UNMIXING

A. Motivation

A neural network autoencoder simply composes of two consecutive information processing layers. Encoder layer transforms input samples to hidden representations while decoder layer tries to restore the original ones from these hidden abstracts with high accuracy. Ultimately, latent correlations in data are unveiled in this chain of the transformations and conserved as trainable parameter sets in the model [41], [42], [43], [44].

Formally, for a given sample $\mathbf{x} \in \mathbb{R}^D$, an autoencoder initially maps it into a hidden representation $\mathbf{y}^1 \in \mathbb{R}^K$ with the inner product of a trainable parameter set \mathbf{W} , \mathbf{b} . Later, the reconstruction of the input sample $\hat{\mathbf{x}} \in \mathbb{R}^D$ is recomputed:

$$\mathbf{y} = f(\mathbf{W}^{(e)} \cdot \mathbf{x} + \mathbf{b}^{(e)}), \quad (2a)$$

$$\hat{\mathbf{x}} = f(\mathbf{W}^{(d)} \cdot \mathbf{y} + \mathbf{b}^{(d)}). \quad (2b)$$

Here \cdot denotes the inner product. $f(\cdot)$ indicates an element-wise nonlinear activation function and a logistic activation function is frequently selected as sigmoid or tanh.

Furthermore, some structural variations are observed for activation functions and/or parameter sets in literature [42], [43], [44], [45]. More clearly, the activation function $f(\cdot)$ at the decoder layer can be discarded or same/disjoint parameter sets can be used for both layers.

Lastly, the parameters are optimized by minimizing standard Euclidean (l_2) reconstruction error of the original and the reconstructed samples:

$$\mathcal{L} = \frac{1}{2} \|\mathbf{x} - \hat{\mathbf{x}}\|_2^2. \quad (3)$$

where \mathcal{L} is the loss function. Fig. 1 visualizes the possible parameter outcomes of a conventional autoencoder learned by Eq. 2a, 2b and 3 on University of Pavia dataset [46].

Current Limitations For Unmixing Problem: The direct usage of a traditional autoencoder might not yield a stable solution particularly for this domain due to several reasons: 1) Logistic functions tend to generate redundant responses even

if the input samples are not correlated with the parameter set [37], [47], [36]. This particularly violates and decreases the sparsity of true projections. 2) Inner product is not sufficiently discriminative and it can lead to erroneous hidden abundances for data. 3) Although the standard Euclidean (l_2) reconstruction term is of main penalty function to minimize the estimation error, it should be carefully regularized with extra terms related to the domain in order to reach to the optimum solution. Otherwise, the solution can be stuck to a local minimum.

For these reasons, these current limitations aggravate conventional autoencoders to attain state-of-the-art performance on hyperspectral unmixing problem.

B. Sparse Autoencoder for Hyperspectral Unmixing

The primary objective of this paper is to accomplish the adaptation of an autoencoder pipeline to the endmember extraction for hyperspectral data. In particular, we strive to preserve the estimation power of autoencoders on latent data correlations as well as the observations that are previously introduced for hyperspectral unmixing.

To enhance the performance and make the autoencoder effective for the problem, we made several modifications in the architecture and the optimization step² as follows. First, bias terms is removed from the formulations due to their adverse effects in the problem. Second, we replace and introduce additional layers to the architecture to improve sparsity as well as consistency. Later, inner product is replaced with spectral angle distance (SAD) to estimate more discriminative hidden abstracts. Finally, we propose a novel loss function to optimize the model parameters effectively. In the following subsections, we will describe these modifications in details.

Zero-biased Filters: In neural network architecture, bias term is one of the critical parameters, especially for linear regression models [48], since it determines the influence of parameters for next layers by thresholding the responses through activation functions. However, bias terms violate one of the crucial properties of endmembers by which none of the materials can be constantly expected in every pixel compositions, if a scene is not composed of one material.

More clearly, since bias terms constantly affect the composition of pixels, they behave like one of the endmembers observed from the data at the end of the optimization step. Fig. 1. plots a possible bias term response for a conventional autoencoder. For this reason, we removed the bias terms in both Eq. 2a and 2b for our model. Also, this step partially retains the simplex set assumption which constitutes a basis for the conventional methods in the literature [3], [4], [5].

Moreover, we discarded the activation function at the decoder layer and intuitively $\mathbf{W}^{(d)}$ parameter begins to represent endmembers \mathbf{E} estimated from a scene (Similarly, hidden abstract \mathbf{y} corresponds to the abundances of a pixel.).

Lastly, since abundance estimates possess non-linear relations and cannot be computed directly from endmembers

¹ \mathbf{y} intuitively corresponds to abundance map per pixel in hyperspectral unmixing.

²Source code and presented results will be available on <https://github.com/savasozkan/endnet>

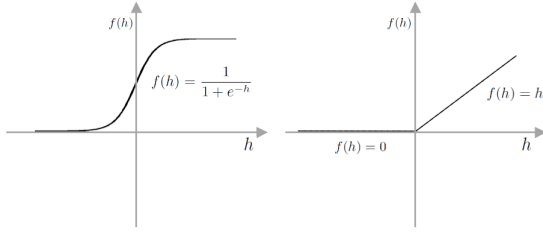


Fig. 2. Response characteristics of Sigmoid (left) and ReLU (right) activation functions.

$\mathbf{W}^{(d)}$, we used disjoint parameter sets for both encoder and decoder layers ($\mathbf{W}^{(e)} \in \mathbb{R}^{K \times D}$ and $\mathbf{W}^{(d)} \in \mathbb{R}^{D \times K}$).

Sparsity and Nonlinearity: Sparsity and nonlinearity are critical features for endmember extraction and hyperspectral unmixing [8], [16], [23], [24] in order to make a robust estimation. As aforementioned limitations, logistic functions are insufficient to conserve the sparsity for the architecture even if they generate nonlinear responses. Therefore, we made three critical modifications in the architecture to achieve sparse, consistent and nonlinear hidden abstracts.

First, a rectified linear activation [37] is used at the encoder layer instead of logistic functions. Fig. 2 illustrates the response characteristics of Sigmoid and Rectified Linear Unit (ReLU) activations for different input values. ReLU basically bounds the negative influence of filters and increases the selectivity of the representation. In addition, it boosts the parameters to saturate more quickly in the optimization step. In the scope of this paper, we tested our method with the variants of rectified activation units [47], [49], [50] to be sure about the optimum solution. These activation units permit limited amount of negative responses to the next layers. However, these negative values ultimately perturb the relation of endmembers (i.e. they become more correlated) and greater than zero constraint (i.e. $y_k > 0$) for the abundance estimates.

However, trainable parameters can instantly become ill-posed (i.e. small changes in the parameters can lead to oscillation and instability in the model) with the removal of the logistic function as expected [38], [51]. Therefore, we introduced a normalization layer [38] before ReLU activation function at the encoder layer. For our model, this layer especially induces selectivity on the top activation responses (it has similar objective as bias term [48]) besides the mitigation of ill-posed effects. It simply normalizes the responses by scaling and reordering them. Fig. 3 illustrates the possible output distribution characteristics of this normalization layer. If we assume that shifting parameter ρ in Eq. 4 is discarded, by combining with ReLU layer, it would permit coarsely 50%

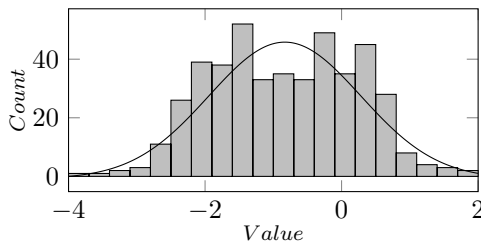


Fig. 3. Distribution characteristic of batch normalization layer outputs. Due to shifting parameter ρ , mean value of the distribution slightly moves to left in the plot. Furthermore, the values that are greater than zero can merely pass to the next layer with the combination of a rectified activation layer.

of the top positive responses to the next layer at each iteration:

$$\text{BN}(\mathbf{h}) = \frac{(\mathbf{h} - \boldsymbol{\mu})}{\sqrt{\boldsymbol{\sigma}^2 + \epsilon}} + \boldsymbol{\rho}, \quad (4)$$

where $\text{BN}(\cdot)$ is the output of the normalization layer and it is fed into ReLU layer in Eq. 5. Also, ϵ is a very small constant (10^{-8}) to prevent zero-division in the formulation. $\mathbf{h} = \mathbf{W}^{(e)} \cdot \mathbf{x}$, $\mathbf{h} \in \mathbb{R}^K$ is the filter response for input \mathbf{x} (We should note that we will redefine this filter response in the following subsection. Here, this formulation is written to preserve the consistency). $\boldsymbol{\mu} = \frac{1}{N} \sum_{i=1}^N \mathbf{x}^{(i)}$, $\boldsymbol{\mu} \in \mathbb{R}^K$ and $\boldsymbol{\sigma}^2 = \frac{1}{N} \sum_{i=1}^N (\mathbf{x}^{(i)} - \boldsymbol{\mu})^2$, $\boldsymbol{\sigma}^2 \in \mathbb{R}^K$ are the mean and variance of mini-batch filter responses at t^{th} iteration. $\boldsymbol{\rho} \in \mathbb{R}^K$ are the trainable parameter to adjust the permutability of filter responses. We should remark that scaling factor in [38] is discarded due to better abundance and endmember extraction:

$$f(\mathbf{h}) = \begin{cases} \text{BN}(\mathbf{h}), & \text{if } \text{BN}(\mathbf{h}) > 0 \\ 0, & \text{otherwise} \end{cases} \quad (5)$$

For ReLU and normalization layer, similar observation can be found in very recent work [36].

However, autoencoders might not still yield the optimum solution in some cases due to parameter overfitting (i.e. lack of full parameter convergence and sparsity). In order to make improvements for reliable abundance estimates and endmembers, we utilized three additional steps at the end of the activation function. For this purpose, we first employed a regularization layer, i.e. Dropout [39], [40] with $\mathbf{r} \sim \text{Bernoulli}(p)$, after the activation function $f(\cdot)$ as $\mathbf{z} = \mathbf{r} * f(\mathbf{h})$. Here $*$ denotes an element-wise product and $0 < p \leq 1$ should be defined by the user based on the spectral correlations of materials in a scene (i.e. if highly correlated materials exist in the scene, p should be close to 0.5). Note that the default value of p is set to 1.0.

Second, we hardly selected top n activations (i.e. highest ones) from \mathbf{z} as similar to [52] (n is fixed to 2 due to the optimum spatial material mixture) to increase the selectivity of $\mathbf{W}^{(d)}$. Finally, we applied $l1$ normalization to satisfy sum-to-one constraint (i.e. $\sum_{k=1}^K y_k = 1$) on abundance estimates:

$$\mathbf{y} = \frac{\mathbf{z}^*}{(\|\mathbf{z}^*\|_1 + \epsilon)}, \quad (6)$$

where \mathbf{z}^* denotes n -top activations. To learn the parameters in our model, we use backpropagation algorithm [53] and Eq. 6 is differentiable except at zero (For this case, partial derivative is directly set to zero). From chain rule, the partial derivative of $l1$ normalization layer is computed as follows:

$$\frac{\partial \mathcal{L}}{\partial \mathbf{z}^*} = \frac{1}{\|\mathbf{z}^*\|_1} \left(\frac{\partial \mathcal{L}}{\partial \mathbf{y}} - \mathbf{y} \sum_{k=1}^K \frac{\partial \mathcal{L}}{\partial y_k} \text{sign}(z_k^*) \right). \quad (7)$$

where \mathcal{L} is the loss function. Also, the term $\frac{\partial \mathcal{L}}{\partial \mathbf{y}}$ defines the propagated error up to the hidden abstracts \mathbf{y} from the upper layer. Lastly, $\text{sign}(\cdot)$ denotes a function which returns the sign of its input.

Discriminative Hidden Abstracts: For neural network autoencoders, input data samples need to be mapped to hidden abstracts truly by storing their latent correlations, in order to recompute the original ones with high accuracy. That's why,

an accurate mapping is of a critical requirement to unveil these latent correlations from data.

Except minor instances [54], inner products of input samples with filter parameters have produced the best performances for almost all applications in visible domain [42], [47], [51]. Especially for hyperspectral domain, there are various useful operators which prove their success on several tasks such as classification and spectral signature comparison [55], [56], [57], [58], [59].

Fig. 4 plots the similarity score distributions of the normalized inner product (first row) and the spectral angle distance (SAD) (second row) of same (blue) and very coherent (red) material spectral signatures. From these plots, it is observed that inner product constantly produces high scores even if different materials are compared. However, same material scores for spectral angle distance (SAD) can be separated from the coherent ones. In addition, [59] explains that SAD is better for separability, while spectral information divergence (SID) is more practical for preserving spectral patterns. Note that separability and discriminative power are especially important to estimate sparse responses at the encoder layer.

For these reasons, we replaced inner product with SAD at the encoder layer to obtain more discriminative and separable hidden abstracts as well as endmembers from hyperspectral data.

Spectral angle distance (SAD) measures the spectral angle between two input samples and a score closer to zero implies higher correlation. One of the concerns addressed for SAD metric [56], [60] is that its limitation to the nonlinear cases. As a remedy, several improvements are presented in literature and most of which are based on kernel-based methods [56], [57], [58]. However, this limitation is not a drawback for our case, since nonlinearity is supplied with the nonlinear activation function [37] and the normalization layer [38] at the output of this metric.

Formally, SAD computes the similarity score of two samples, $\mathbf{x}^{(i)}$ and $\mathbf{x}^{(j)}$, as follows:

$$S(\mathbf{x}^{(i)}, \mathbf{x}^{(j)}) = \cos^{-1}(\theta(\mathbf{x}^{(i)}, \mathbf{x}^{(j)})), \quad (8)$$

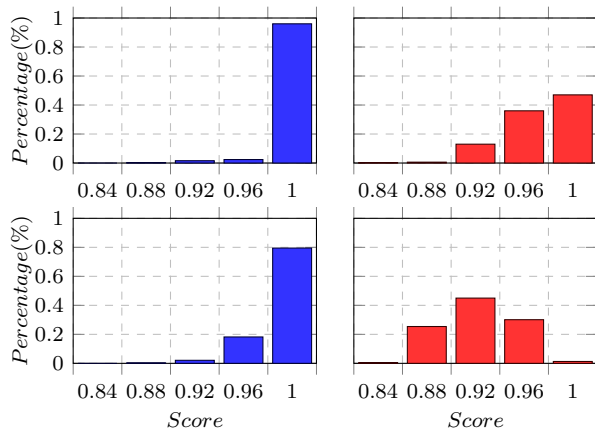


Fig. 4. Normalized similarity score distributions for same (blue) and very coherent (red) class comparisons with inner product (first row) and spectral angle distance (second row). As can be seen from the plots, spectral angle distance obtain more discriminative results.

where

$$\theta(\mathbf{x}^{(i)}, \mathbf{x}^{(j)}) = \frac{\mathbf{x}^{(i)} \cdot \mathbf{x}^{(j)}}{\|\mathbf{x}^{(i)}\|_2 \|\mathbf{x}^{(j)}\|_2}. \quad (9)$$

In Eq. 8, score varies between $[0, \pi]$ and zero value means that two samples are identical. Therefore, we first need to normalize the score $S(\cdot, \cdot)$ to $[0, 1]$, since higher score means higher similarity at the decoder layer:

$$C(\mathbf{x}^{(i)}, \mathbf{x}^{(j)}) = 1.0 - \frac{S(\mathbf{x}^{(i)}, \mathbf{x}^{(j)})}{\pi}. \quad (10)$$

From this moment on, we reformulate the filter responses as $\mathbf{h} = C(\mathbf{x}, \mathbf{W}^{(e)})$. Similarly, SAD is differentiable to optimize necessary parameters with the backpropagation algorithm by minimizing the loss function \mathcal{L} . By applying chain rule again, the gradient of k^{th} row \mathbf{w}_k of $\mathbf{W}^{(e)}$, $\mathbf{w}_k \in \mathbb{R}^{1 \times D}$ can be computed as:

$$\frac{\partial \mathcal{L}}{\partial \mathbf{w}_k} = \frac{\partial \mathcal{L}}{\partial C_k} \frac{\partial C_k}{\partial S_k} \frac{\partial S_k}{\partial \theta_k} \frac{\partial \theta_k}{\partial \mathbf{w}_k}, \quad k = 1, 2, \dots, K. \quad (11)$$

where C_k , S_k and θ_k are the simplifications of $C(\mathbf{x}, \mathbf{w}_k)$, $S(\mathbf{x}, \mathbf{w}_k)$ and $\theta(\mathbf{x}, \mathbf{w}_k)$ respectively to ease the formulation and understandability. Also, each derivation term in Eq. 11 can be written as:

$$\frac{\partial C_k}{\partial S_k} = \frac{-1}{\pi}, \quad (12a)$$

$$\frac{\partial S_k}{\partial \theta_k} = \frac{-1}{\sqrt{1 - \theta_k^2}}, \quad (12b)$$

$$\frac{\partial \theta_k}{\partial \mathbf{w}_k} = \frac{\mathbf{x}}{\|\mathbf{w}_k\|_2 \|\mathbf{x}\|_2} - \frac{\mathbf{w}_k * (\mathbf{w}_k \cdot \mathbf{x})}{\|\mathbf{w}_k\|_2^3 \|\mathbf{x}\|_2}. \quad (12c)$$

In the next subsection, we will analyze the optimization step of our method by introducing modifications in the objective function.

Learning: Parameter optimization aims to minimize the error between input samples and their reconstructed versions by learning useful latent correlations from data. However, we found out that use of Euclidean (l_2) norm as a primary objective term to unveil these correlations is not completely adequate for the problem. The main limitation of Euclidean norm is that it aggravates the method by estimating inappropriate/underestimated endmembers under severe illumination changes [61]. On the other hand, spectral angle distance-like (SAD) operator overcomes these limitations and improves unmixing performances by exploiting geometric features of samples as explained in [28], [62]. In addition, smoothness and sparsity priors should be considered in the loss function for better parameter convergence. For this purpose, we made a critical set of modifications in the objective function related to this domain and a novel objective function \mathcal{L} is reformulated as:

$$\mathcal{L} = \frac{\lambda_0}{2} \|\mathbf{x} - \hat{\mathbf{x}}\|_2^2 - \lambda_1 D_{KL}(1.0 \| C(\mathbf{x}, \hat{\mathbf{x}})) + \lambda_2 \|\mathbf{z}\|_1 + \lambda_3 \|\mathbf{W}^{(e)}\|_2 + \lambda_4 \|\mathbf{W}^{(d)}\|_2 + \lambda_5 \|\boldsymbol{\rho}\|_2 \quad (13)$$

where $C(\cdot, \cdot)$ is the normalized SAD score between the original and reconstructed version as in Eq. 10. λ_0 is the term that controls the influence of Euclidean norm. Additionally,

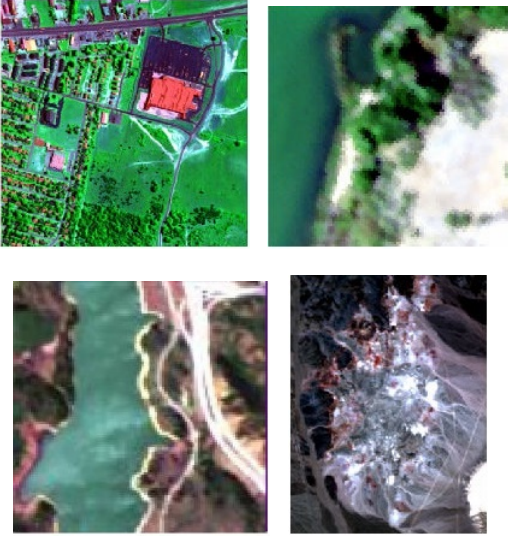


Fig. 5. Four real hyperspectral datasets used in the experiments: Urban, Samson, Jasper Ridge and Cuprite respectively. These datasets are broadly used to evaluate the performance of a method for endmember extraction and abundances unmixing from hyperspectral data.

we add Kullback-Leibler divergence term (D_{KL}) [63], [64] to maximize SAD score distributions between the original and the reconstructed samples. λ_1 determines the effect of this cost term to the objective function. Note that Euclidean norm term is still critical for stable estimates and it cannot be directly set to zero, contrary to [36]. Thus, we empirically set λ_0 and λ_1 to 0.01 and 10 respectively.

Moreover, sparsity at the loss function is essential for effective hyperspectral unmixing, even if the architecture enforces it too. Therefore, we introduce a l_1 regularization term $\|\mathbf{z}\|_1$ as in [65] which penalizes the hidden layers that constantly generate responses for different input samples. Thus, sparsity is enforced to the hidden abstracts and more distinct filter parameters are obtained for each material. The influence of l_1 sparsity term λ_2 is tuned to 0.1 which is a relatively large value. But, we should note that this value needs to be increased/decreased depending on the mixture level of a scene.

As aforementioned, we also add l_2 smoothing terms to the objective function for each trainable parameter and we define their values as 10^{-5} , 10^{-5} and 10^{-3} for λ_3 , λ_4 and λ_5 respectively.

The model parameters are optimized with a gradient-based stochastic Adam [66] optimizer by minimizing the loss function. We fixed learning rate and number of training iterations to 0.001 and 400K respectively for all datasets (These terms can still be tuned). Additionally, mini-batch size N is set to 64 to balance the accuracy and the complexity at each iteration. Unlike the suggested values for momentum terms as in [66], we empirically found out that β_1 value should be defined as 0.7 to reduce the oscillation and instability of learning in the model.

Lastly, the parameters ($\mathbf{W}^{(e)}$ and $\mathbf{W}^{(d)}$) are initialized with the estimates of VCA-like methods [3], [6], [27] instead of random initialization. This approach provides several advantages: First, it is practical to start the optimization from a more reliable initialization which can span all data points to decrease the possibility of parameter overshooting (if any geometrical

volume-based algorithm is used). Second, it speeds up the convergence of the parameters.

Prevent Autoencoder From Overfitting: As mentioned, we utilized Dropout [39], [40] at the hidden layer to prevent hidden abstracts from overfitting to a poor quality solution. In addition, we employ denoising autoencoder scheme [41] in the parameter optimization step to be robust to noise exhibited on data (i.e. approximation error η in the process). Even if the primary principles for both methods are similar, we used these methods at different layers to generalize our model parameters.

This scheme is essentially based on the fact that data samples are initially corrupted with an additive Gaussian noise on purpose while the reconstruction error is computed over the original ones. It helps to improve the generalization capacity of the encoder parameter set and it leads to better solution for robust representations by considering possible deformations (i.e. illumination changes, sensor noise etc.) in advance.

In practice, we opt to utilize such corruption process that does not hurt hidden responses significantly. This is particularly important since SAD is sensitive to large variations. For this purpose, isotropic Gaussian noise ($\tilde{\mathbf{x}}|\mathbf{x} \sim \mathcal{N}(\mathbf{x}|0, \sigma^2)$) and mask noise (i.e. it randomly chooses a portion of the elements) are jointly used to perturb the data. Additionally, we limit the mask noise to alter at most 40% of the original elements with the additive noise. However, the value of this parameter can be reduced for noisy data [46]. Fig. 6 visualizes the original spectral signatures and their corrupted versions under this assumption.

C. Fractional Abundance Estimation

After the endmember extraction, we need to find the abundances of each material on data pixels. In our method, we can obtain these values in two different ways.

- We can use the hidden abstracts \mathbf{y} of our model for each sample.
- Also, we can solve an inverse problem with the estimated endmembers $\mathbf{W}^{(d)}$ since the decoder layer is linear.

As explained in [67], due to the averaging operations for mean and variance values in batch normalization, hidden abstracts tend to generate different responses in test time and it can affect the accuracy of estimates. Therefore, we adapt Simplex Projection Unmixing (SPU) [27], [68] algorithm with SAD kernel for abundance map estimation. This algorithm basically estimates the abundances by using the mutual distances of material spectral signatures and data samples. It also assumes that nonnegativity and sum-to-one constraints are preserved in the nonlinear solution.

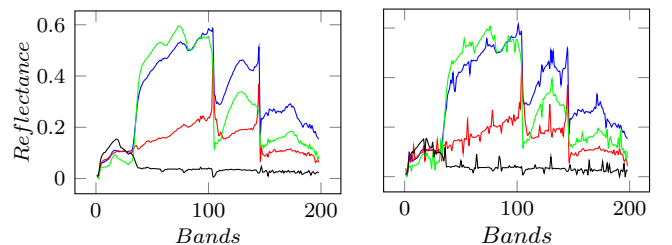


Fig. 6. Four samples corrupted with the denoising criterion. Color is discriminative for hyperspectral signature pairs.

TABLE I
SAD AND RMSE RESULTS ON URBAN DATASET. THE MEAN AND STANDARD DEVIATION ARE REPORTED FOR EACH METHOD. THE BEST RESULTS ARE ILLUSTRATED IN BOLD.

Endm.	Spectral Angle Distance (SAD) ($\times 10^{-2}$)								EndNet-DMaxD
	VCA	DMaxD	MVSA	SPICE	SCM	$l_{1 2}$ -NMF	DgS-NMF	EndNet-VCA	
#1	21.56 \pm 3.1	13.16 \pm 0.0	19.04 \pm 0.1	45.04 \pm >9	9.38 \pm 0.0	6.06 \pm 0.2	5.86 \pm 0.1	6.72 \pm 0.2	6.88 \pm 0.2
#2	39.04 \pm 5.1	>99 \pm 0.0	>99 \pm 1.3	>99 \pm >9	10.55 \pm 0.0	20.05 \pm 0.4	13.69 \pm 0.4	4.04 \pm 0.1	3.92 \pm 0.3
#3	26.77 \pm 7.5	7.43 \pm 0.0	37.83 \pm 9.4	30.89 \pm >9	14.03 \pm 0.0	3.71 \pm 0.0	4.12 \pm 0.0	3.68 \pm 0.2	3.53 \pm 0.1
#4	82.39 \pm 0.1	21.74 \pm 0.0	18.41 \pm 1.9	66.37 \pm >9	41.86 \pm 0.0	14.22 \pm 0.2	10.54 \pm 0.3	3.99 \pm 0.7	3.35 \pm 0.5
Avg.	41.77 \pm 4.5	37.88 \pm 0.0	43.81 \pm 3.1	60.57 \pm >9	18.79 \pm 0.0	11.01 \pm 0.2	8.55 \pm 0.2	4.60 \pm 0.3	4.42 \pm 0.3
	Root Mean Square Error (RMSE) ($\times 10^{-2}$)								EndNet-DMaxD
	VCA	DMaxD	MVSA	SPICE	SCM	$l_{1 2}$ -NMF	DgS-NMF	EndNet-VCA	
#1	34.40 \pm 8.5	36.09 \pm 0.0	29.80 \pm 0.4	29.43 \pm 3.4	32.79 \pm 0.0	14.77 \pm 0.1	13.18 \pm 0.1	10.24 \pm 0.1	10.41 \pm 0.2
#2	42.86 \pm 5.2	42.85 \pm 0.0	33.96 \pm 0.0	35.32 \pm 4.5	36.25 \pm 0.0	16.16 \pm 0.2	12.95 \pm 0.0	13.01 \pm 0.3	12.24 \pm 0.3
#3	31.09 \pm 6.0	33.79 \pm 0.0	30.81 \pm 0.5	26.33 \pm 1.9	32.61 \pm 0.0	12.65 \pm 0.2	9.57 \pm 0.1	8.69 \pm 0.3	8.35 \pm 0.3
#4	18.81 \pm 1.7	21.03 \pm 0.0	18.38 \pm 0.3	21.93 \pm 6.9	32.86 \pm 0.0	6.90 \pm 0.1	6.27 \pm 0.0	6.13 \pm 0.2	5.92 \pm 0.1
Avg.	31.79 \pm 5.3	33.44 \pm 0.0	28.23 \pm 0.3	28.25 \pm 4.2	33.59 \pm 0.0	12.62 \pm 0.1	10.49 \pm 0.1	9.51 \pm 0.2	9.23 \pm 0.2

In particular, the estimation of the abundances by solving an inverse problem with $\mathbf{W}^{(d)}$ and SPU empirically introduces further improvements to the performance, even if estimated hidden abstracts \mathbf{y} still yield compatible results. Thus, the reported results for abundance maps are estimated by the combination of these methods.

However, the proposed method should be considered as spectral unmixing method as well as endmember extractor, since it optimizes the loss function jointly. We conduct additional experiments to analysis the abundance map performances and you can find further details about these comparisons at Section III. C.

III. EXPERIMENTS

Here, we demonstrate the performance of our method on several datasets. For this purpose, we report quantitative and qualitative results of our method on hyperspectral unmixing problem. Also, the estimated spectral signatures and the abundance maps are compared with the corresponding ground truth.

In the beginning of this section, we will summarize the details of publicly available datasets, baseline methods and evaluation metrics that we use in the experiments. Lastly, we summarize the parameter settings determined in the experiments.

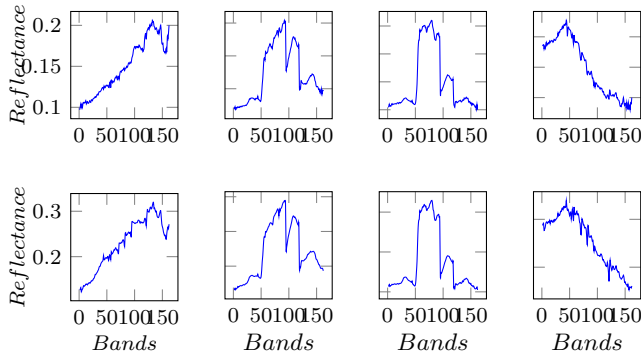


Fig. 7. Endmember signatures (Asphalt, Grass, Tree and Roof) on Urban dataset for ground truth (first row) and EndNet-DMaxD (second row).

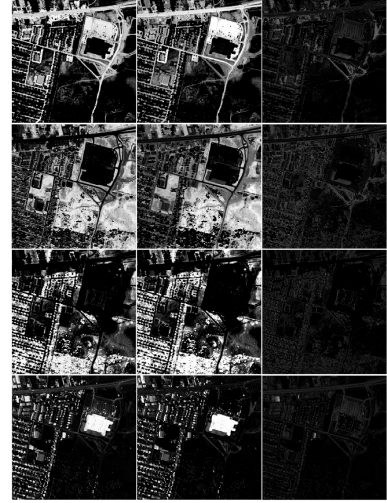


Fig. 8. Abundance map on Urban dataset with EndNet-DMaxD method. Each row corresponds to four materials: Asphalt, Grass, Tree and Roof respectively. Also, each column indicates estimated abundance results, ground truth and the absolute differences of the abundance results and the ground truth for the corresponding materials.

A. Hyperspectral Datasets

In order to make fair comparisons, we evaluate the proposed method on well-known and extensively used datasets for end-member extraction [69], [70], [71], [72], [46], [73], [74], [75], [7]. (Please look at their references for further details about these datasets.) Moreover, even if synthetic data is reliable to precisely measure the true abundance maps/endmembers, it is nearly impossible to simulate some extreme cases such as non-linearity on data. Therefore, all experiments are conducted on real datasets to show the effectiveness of the method. (You can also find additional quantitative results on the project website.) **Urban [69], [70]:** The pixel resolution of data is 307×307 . Several channels (1-4, 76, 87, 101-111, 136-153 and 198-210) are removed due to water-vapor absorption and atmospheric effects. There are four constituent materials: Asphalt (#1), Grass (#2), Tree (#3), Roof (#4).

Samson [70]: Data is generated by SAMSON sensor. It contains 156 channels and covers the spectral range from 0.4 to $0.9\mu\text{m}$. In order to make fair comparisons, a subimage of the original data (95×95) is considered as in [70]. Three

TABLE II

SAD AND RMSE RESULTS ON SAMSON DATASET. THE MEAN AND STANDARD DEVIATION ARE REPORTED FOR EACH METHOD. THE BEST RESULTS ARE ILLUSTRATED IN BOLD.

Endm.	Spectral Angle Distance (SAD) ($\times 10^{-2}$)								
	VCA	DMaxD	MVSA	SPICE	SCM	$l_{1 2}$ -NMF	DgS-NMF	EndNet-VCA	EndNet-DMaxD
#1	22.33 \pm 2.7	4.04 \pm 0.0	4.19 \pm 0.0	45.37 \pm >9	1.74 \pm 0.0	6.21 \pm 7.3	5.64 \pm 7.4	1.32 \pm 0.2	1.29 \pm 0.1
#2	4.90 \pm 0.2	2.19 \pm 0.0	5.61 \pm 0.0	12.19 \pm >9	3.15 \pm 0.0	5.23 \pm 0.3	4.80 \pm 0.3	4.72 \pm 0.2	4.69 \pm 0.1
#3	12.29 \pm 0.0	13.04 \pm 0.0	18.15 \pm 0.0	9.24 \pm >9	25.28 \pm 0.0	11.97 \pm 2.1	4.7 \pm 0.3	3.36 \pm 0.2	2.95 \pm 0.3
Avg.	13.17 \pm 1.0	6.42 \pm 0.0	9.31 \pm 0.0	22.26 \pm >9	10.05 \pm 0.0	7.80 \pm 3.2	5.05 \pm 2.7	3.13 \pm 0.2	2.98 \pm 0.2
	Root Mean Square Error (RMSE) ($\times 10^{-2}$)								
	VCA	DMaxD	MVSA	SPICE	SCM	$l_{1 2}$ -NMF	DgS-NMF	EndNet-VCA	EndNet-DMaxD
#1	29.98 \pm >9	25.70 \pm 0.0	21.50 \pm 0.0	27.76 \pm >9	18.44 \pm 0.0	8.58 \pm 3.3	7.77 \pm 3.8	5.86 \pm 0.0	5.72 \pm 0.0
#2	26.81 \pm 6.5	32.20 \pm 0.0	25.12 \pm 0.0	28.16 \pm 2.8	20.75 \pm 0.0	7.44 \pm 3.7	7.74 \pm 3.6	4.15 \pm 0.1	3.84 \pm 0.1
#3	28.75 \pm 2.7	39.81 \pm 0.0	35.70 \pm 0.0	35.57 \pm 3.4	33.95 \pm 0.0	5.55 \pm 0.9	2.70 \pm 0.9	2.07 \pm 0.0	2.11 \pm 0.0
Avg.	28.51 \pm 6.3	32.57 \pm 0.0	27.44 \pm 0.0	30.49 \pm 5.4	24.38 \pm 0.0	7.19 \pm 2.4	6.07 \pm 2.8	4.01 \pm 0.0	3.88 \pm 0.0

material types are observed in the scene: Soil (#1), Tree (#2) and Water (#3).

Jasper Ridge [71]: Data is captured by AVIRIS sensor. A subimage of 100×100 pixels of the original data is used. Some of the channels (1-3, 108-112, 154-166 and 220-224) are discarded due to the atmospheric effects and water-vapor absorption. Tree (#1), Water (#2), Soil (#3) and Road (#4) are observed in the scene.

Cuprite [69], [70], [72]: Data is captured with AVIRIS over Cuprite, Nevada. It has 188 spectral reflectance bands covering the wavelength range from 0.4 to 2.5 μm . It has a nominal ground resolution of 20 m and a spectral resolution of 10 nm. A subimage of the original data [70] (250×190 pixels) is considered. Noisy (1-2 and 221-224) and water-vapor absorption (104-113 and 148-167) channels are also removed from data. This dataset hosts 12 unique mineral spectral signatures: Alunite (#1), Andradite (#2), Buddingtonite (#3), Dumortierite (#4), Kaolinite₁ (#5), Kaolinite₂ (#6), Muscovite (#7), Montmorillonite (#8), Nontronite (#9), Pyrope (#10), Sphepe (#11) and Chalcedony (#12).

University of Pavia [46]: Data is recorded by ROSIS sensor over Pavia, Italy. The spectral band number is 103 and the spectral range is varied from 0.43 to 0.86 μm . The spatial pixel resolution is 610×340 and the ground resolution is approximately 1.3 m. It comprises 9 labeled classes that covers different man-made structures and natural objects. Since bricks-gravel and asphalt-bitumen have similar spectral signatures, we considered these classes as joint classes as claimed in [75]. In the experiment, 7 labeled classes are used: Asphalt-Bitumen (#1), Meadows (#2), Trees (#3), Metal Sheets (#4), Bare Soil (#5), Gravel-Bricks (#6) and Shadow (#7).

Mississippi Gulfport [73]: Data is collected from University of Southern Mississippi-Gulfpark Campus. It has 64 spectral reflectance bands covering the wavelength range from 0.368 to 1.043 μm . The spatial resolution of the data is 1 m. It contains 11 man-made structures and natural materials. We eliminated sidewalk, yellow curb, cloth panels and water classes due to the lack of sufficient amounts of data samples. The remaining classes are used in the experiments: Trees (#1), Grass Pure (#2), Grass Ground (#3), Dirt & Sand (#4), Road (#5), Shadow (#6) and Building (#7).

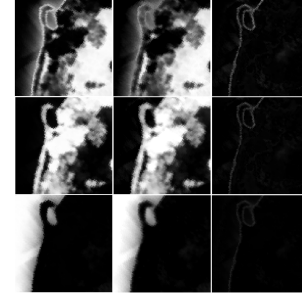


Fig. 9. Abundance map on Samson dataset with EndNet-DMaxD method. Results for three materials, Soil, Tree and Water, are reported in different rows. Estimated abundance maps, ground truth and absolute differences of the abundance maps and the ground truth are illustrated in columns respectively.

B. Baselines, Metrics and Parameter Settings

Baselines: We compare our proposed method, EndNet, with several open-source hyperspectral unmixing algorithms throughout this study:

- Vertex Component Analysis (VCA) [3] (the code is available on <http://www.lx.it.pt/biucas/code.htm>)
- Minimum Volume Simplex Analysis (MVSA) [14] (the code is available on <http://www.lx.it.pt/biucas/code.htm>)
- Sparsity Promoting Iterated Constrained Endmembers (SPICE) [74] (the code is available on <https://github.com/GatorSense/SPICE>)
- Spatial Compositional Model (SCM) [75] (the code is available on <https://github.com/zhouyuanxvcv/Hyperspectral>)
- Distance-MaxD (DMaxD) [7] (the code is available on <https://sites.google.com/site/robheyleenresearch/code>)

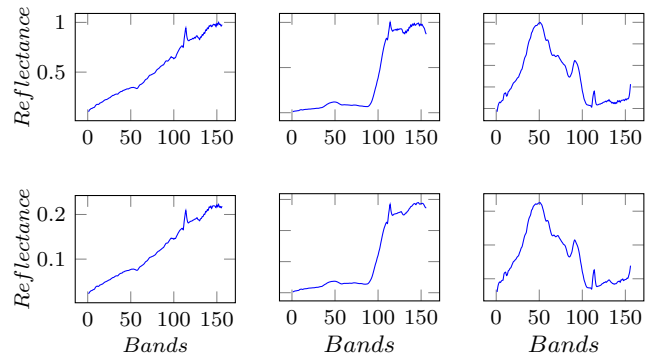


Fig. 10. Endmember signatures (Soil, Tree and Water) on Samson dataset for ground truth (first row) and EndNet-DMaxD (second row).

TABLE III

SAD AND RMSE RESULTS ON JASPER RIDGE DATASET. THE MEAN AND STANDARD DEVIATION ARE REPORTED FOR EACH METHOD. THE BEST RESULTS ARE ILLUSTRATED IN BOLD.

Endm.	Spectral Angle Distance (SAD) ($\times 10^{-2}$)								
	VCA	DMaxD	MVSA	SPICE	SCM	$l_{1 2}$ -NMF	DgS-NMF	EndNet-VCA	EndNet-DMaxD
#1	24.34 \pm 5.3	15.58 \pm 0.0	18.41 \pm 1.2	40.95 \pm 9	6.53 \pm 0.0	15.10 \pm 0.3	4.66 \pm 0.2	8.23 \pm 3.1	4.99 \pm 0.4
#2	25.21 \pm 0.4	25.39 \pm 0.0	>99 \pm 1.0	59.83 \pm 9	10.80 \pm 0.0	4.60 \pm 0.0	4.60 \pm 0.0	3.62 \pm 0.4	4.23 \pm 0.9
#3	34.81 \pm 9	13.35 \pm 0.0	26.27 \pm 0.7	28.03 \pm 9	21.25 \pm 0.0	6.16 \pm 0.5	5.66 \pm 0.2	6.23 \pm 0.7	4.47 \pm 0.3
#4	50.56 \pm 9.3	10.69 \pm 0.0	7.01 \pm 0.8	86.19 \pm 9	11.58 \pm 0.0	9.81 \pm 0.1	6.73 \pm 0.1	67.06 \pm 0.5	1.96 \pm 0.2
Avg.	33.73 \pm 6.2	16.25 \pm 0.0	37.92 \pm 0.9	53.75 \pm 9	12.54 \pm 0.0	7.19 \pm 2.4	5.41 \pm 0.1	21.29 \pm 1.2	3.91 \pm 0.5
	Root Mean Square Error (RMSE) ($\times 10^{-2}$)								
	VCA	DMaxD	MVSA	SPICE	SCM	$l_{1 2}$ -NMF	DgS-NMF	EndNet-VCA	EndNet-DMaxD
#1	22.47 \pm 8.9	15.94 \pm 0.0	21.65 \pm 0.3	22.05 \pm 6.9	23.87 \pm 0.0	16.16 \pm 0.5	11.66 \pm 0.2	8.19 \pm 2.6	8.24 \pm 0.4
#2	24.09 \pm 2.0	11.31 \pm 0.0	24.54 \pm 0.8	27.08 \pm 9	13.30 \pm 0.0	5.57 \pm 0.0	4.13 \pm 0.0	26.18 \pm 0.5	6.17 \pm 0.3
#3	30.50 \pm 9.3	17.73 \pm 0.0	21.11 \pm 2.0	21.35 \pm 5.8	28.47 \pm 0.0	17.02 \pm 0.4	11.13 \pm 0.3	19.91 \pm 0.9	8.98 \pm 0.2
#4	29.60 \pm 4.6	20.00 \pm 0.0	12.72 \pm 0.2	27.44 \pm 9	19.87 \pm 0.0	6.73 \pm 0.2	5.68 \pm 0.1	30.65 \pm 0.3	8.55 \pm 0.1
Avg.	26.66 \pm 6.2	16.24 \pm 0.0	20.00 \pm 0.8	24.48 \pm 8.1	23.04 \pm 0.0	11.37 \pm 0.2	8.15 \pm 0.2	21.22 \pm 1.1	7.96 \pm 0.3

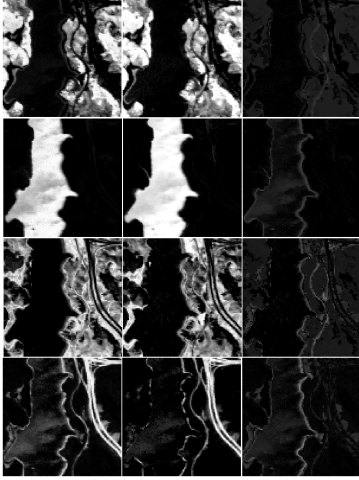


Fig. 11. Estimated abundance maps and the absolute differences with the ground truth on Jasper Ridge dataset for EndNet-DMaxD method. Four materials, Tree, Water, Soil and Road, are illustrated in different rows.

In addition to these open-source algorithms, we report the performances of recent methods for several datasets by referring directly to their reported scores, since their codes are not available: $l_{1|2}$ -NMF [69], [70], DgS-NMF [70]. Particularly, we should note that we compare our method with the method like DgS-NMF [70] to show that our method outperforms even the methods that exploit spatial priors in their solution.

Metrics: To evaluate the unmixing performance and compare with ground truth, we utilize two metrics: Spectral Angle

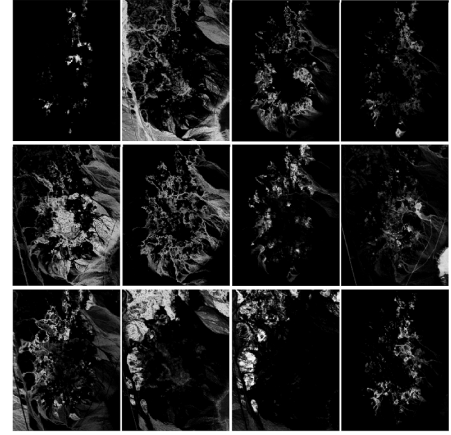


Fig. 13. Estimated abundance results on Cuprite dataset with EndNet-DMaxD method. First Row: Alunite, Andradite, Buddingtonite, Dumortierite, Kaolinite₁, Kaolinite₂. Second Row: Muscovite, Montmorillonite, Nontronite, Pyrope, Sphehne, Chalcedony.

Distance (SAD) and Root Mean Square Error (RMSE):

$$\text{SAD}(\mathbf{e}, \hat{\mathbf{e}}) = \cos^{-1} \left(\frac{\mathbf{e} \cdot \hat{\mathbf{e}}}{\|\mathbf{e}\|_2 \|\hat{\mathbf{e}}\|_2} \right), \quad (14)$$

As mentioned earlier, SAD is used to evaluate the quality of estimated endmember with ground truth by measuring angle distance. Similarly, to assess the accuracy of the estimated abundances, we utilized RMSE metric as:

$$\text{RMSE}(\mathbf{y}, \hat{\mathbf{y}}) = \sqrt{\frac{1}{N} \|\mathbf{y} - \hat{\mathbf{y}}\|_2^2}. \quad (15)$$

Note that smaller values indicate better performances for both metrics.

Parameter Settings: For parameter settings, we fixed the default parameter values of the baseline methods in our experiments. Differently, we tuned the parameters of SCM algorithm for each dataset based on the observations in [75].

For abundance map estimation, we selected Fully-Constrained Least Square (FCLS) for MVSA while Simplex Projection Unmixing (SPU) with l_2 kernel is determined for VCA and DMaxD algorithms. SPICE and SCM compute the optimum abundances for the scene in their algorithms.

For our method, three parameters should be tuned by the user for different scenes, namely p in the dropout layer, λ_2 in

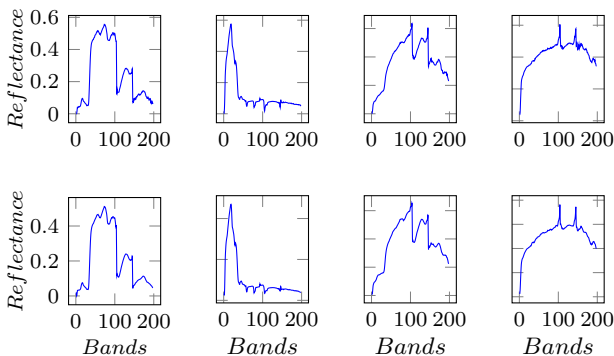


Fig. 12. Endmember signatures (Tree, Water, Soil and Road) on Jasper dataset for ground truth (first row) and EndNet-DMaxD (second row).

TABLE IV
SAD RESULTS ON CUPRITE DATASET. THE MEAN AND STANDARD DEVIATION ARE REPORTED FOR EACH METHOD. THE BEST RESULTS ARE ILLUSTRATED IN BOLD.

Endm.	Spectral Angle Distance (SAD) ($\times 10^{-2}$)								
	VCA	DMaxD	MVSA	SPICE	SCM	$l_{1 2}$ -NMF	DgS-NMF	EndNet-VCA	EndNet-DMaxD
#1	12.89 \pm 5.3	8.58 \pm 0.0	23.60 \pm 5.7	14.71 \pm 1.6	24.43 \pm 4.6	16.22 \pm 2.0	12.48 \pm 1.8	13.60 \pm 2.9	14.18 \pm 2.5
#2	8.21 \pm 1.9	7.15 \pm 0.0	>99 \pm >9	9.32 \pm 1.6	7.19 \pm 0.2	10.15 \pm 3.0	7.59 \pm 1.2	7.65 \pm 0.1	7.34 \pm 0.2
#3	9.04 \pm 2.0	11.58 \pm 0.0	>99 \pm >9	10.26 \pm 0.3	13.25 \pm 0.3	12.50 \pm 7.5	10.81 \pm 3.2	11.44 \pm 0.8	11.66 \pm 1.1
#4	9.51 \pm 3.0	8.01 \pm 0.0	38.36 \pm >9	11.91 \pm 1.3	12.22 \pm 0.9	13.07 \pm 5.3	11.01 \pm 2.1	8.38 \pm 0.6	7.81 \pm 0.7
#5	8.88 \pm 1.5	8.47 \pm 0.0	25.44 \pm 6.2	13.09 \pm 2.7	9.20 \pm 1.3	9.42 \pm 1.8	9.02 \pm 2.9	12.06 \pm 0.9	13.16 \pm 1.1
#6	7.08 \pm 5.2	8.52 \pm 0.0	>99 \pm >9	9.60 \pm 0.5	6.80 \pm 0.4	9.82 \pm 2.7	7.42 \pm 1.2	6.05 \pm 0.3	5.69 \pm 0.2
#7	17.13 \pm 4.0	10.26 \pm 0.0	41.73 \pm >9	9.97 \pm 0.5	17.15 \pm 2.5	29.86 \pm 7.4	20.51 \pm 6.0	15.93 \pm 1.9	15.45 \pm 1.1
#8	6.22 \pm 0.4	6.19 \pm 0.0	81.84 \pm >9	8.60 \pm 0.5	6.28 \pm 0.2	10.27 \pm 4.7	7.27 \pm 1.2	5.51 \pm 0.3	5.75 \pm 0.1
#9	7.95 \pm 1.0	7.36 \pm 0.0	65.95 \pm >9	11.45 \pm 1.6	7.61 \pm 0.1	12.80 \pm 4.1	8.88 \pm 1.7	8.36 \pm 0.7	7.78 \pm 0.1
#10	11.11 \pm 4.5	13.08 \pm 0.0	88.65 \pm >9	6.99 \pm 1.9	5.89 \pm 0.1	8.12 \pm 1.9	8.82 \pm 5.0	5.87 \pm 0.5	6.12 \pm 0.4
#11	8.40 \pm 5.9	28.56 \pm 0.0	52.02 \pm >9	8.99 \pm 2.4	7.11 \pm 1.7	11.03 \pm 3.3	8.15 \pm 2.1	9.03 \pm 1.4	8.38 \pm 1.2
#12	10.07 \pm 4.5	8.23 \pm 0.0	9.10 \pm 1.35	8.63 \pm 0.9	9.29 \pm 0.2	13.72 \pm 6.0	13.62 \pm 6.3	10.56 \pm 1.6	11.14 \pm 0.9
Avg.	9.71 \pm 2.9	10.54 \pm 0.0	71.92 \pm >9	10.30 \pm 1.3	10.54 \pm 1.0	13.07 \pm 4.1	10.46 \pm 2.9	9.53 \pm 1.0	9.54 \pm 0.8

the optimization step and the percentage of mask noise. We will redefine the values of these parameter if the scene needs to be tuned by presenting reasonable explanations. Otherwise, the default values are used on each dataset ($p = 1.0$, $\lambda_2 = 0.1$ and 40% mask noise). Also, EndNet-VCA and EndNet-DMaxD in the experiments denote that which of the algorithms is used in the parameter initialization of our method.

Finally, for an estimated endmember, corresponding ground truth material (i.e. most similar ground truth material) is determined by measuring their highest responded SAD similarity score in the experiments.

Computational Complexity: Speed and memory requirement are two additional important parameters for the problem. Since our method is solved with a stochastic gradient-based solver, it practically scales the problem for large-scale data. Moreover, compared to SCM [75], the proposed method yields similar results for the computation time. However, note that the method can be easily parallelized on Graphical Processing Units (GPUs) due to the neural network architecture.

C. Experiments on Hyperspectral Unmixing Datasets

In this section, we compare our method with the baselines on Urban, Samson, Jasper Ridge and Cuprite datasets. These four datasets are illustrated in Fig. 5. For reliable assessments, tests are repeated 20 times for each method, thus mean and standard deviation of the results are reported. We also

TABLE V
COMPARISON OF ABUNDANCE MAP ESTIMATION RESULTS FOR SPU (FIRST ROWS) AND ENDNET-DMAXD (SECOND ROWS).

Root Mean Square Error (RMSE) ($\times 10^{-2}$)			
	Urban	Samson	Jasper
#1	SPU: 10.41 \pm 0.2	SPU: 5.72 \pm 0.0	SPU: 8.24 \pm 0.4
	EndN: 13.04 \pm 0.3	EndN: 9.41 \pm 0.1	EndN: 10.12 \pm 0.6
#2	SPU: 12.24 \pm 0.3	SPU: 3.84 \pm 0.1	SPU: 6.17 \pm 0.3
	EndN: 14.43 \pm 0.3	EndN: 6.47 \pm 0.3	EndN: 11.48 \pm 0.8
#3	SPU: 8.35 \pm 0.3	SPU: 2.11 \pm 0.0	SPU: 8.19 \pm 0.2
	EndN: 8.71 \pm 0.5	EndN: 3.93 \pm 0.1	EndN: 9.53 \pm 0.3
#4	SPU: 5.92 \pm 0.2	-	SPU: 8.55 \pm 0.1
	EndN: 7.59 \pm 0.2	-	EndN: 12.29 \pm 0.4
Avg.	SPU: 9.23 \pm 0.2	SPU: 3.88 \pm 0.0	SPU: 7.96 \pm 0.3
	EndN: 10.94 \pm 0.4	EndN: 5.72 \pm 0.2	EndN: 10.85 \pm 0.6

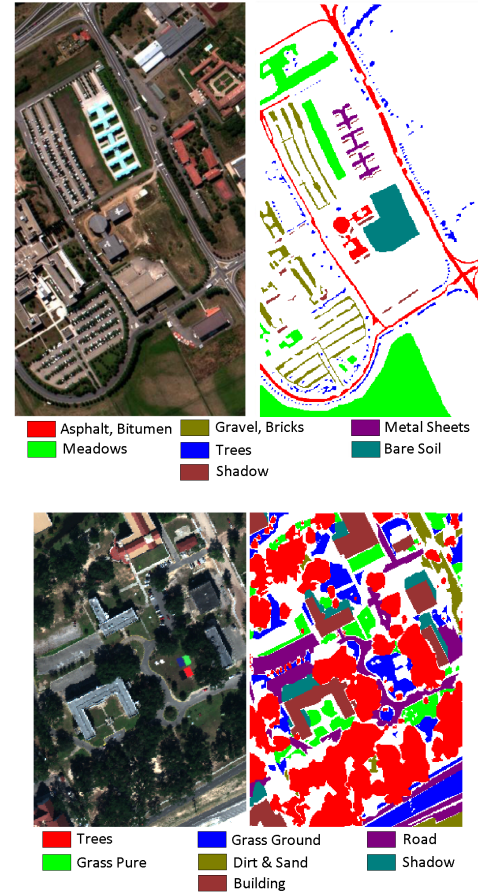


Fig. 14. Two real hyperspectral datasets with pixel-wise class labels: University of Pavia and Mississippi Gulfport respectively.

illustrate the qualitative results of our method to provide visual comparisons on the estimated abundance maps.

In Tables I, II and III, each row corresponds to SAD or RMSE performances of different methods for a single material. Also, the last row at each table denotes the average performance of all materials for the corresponding metric. In Table IV, the SAD performances are only reported since Cuprite dataset does not have a quantitative abundance map ground truth. Fig. 8, 9, 11 and 13 visualize the qualitative abundance performances of our EndNet-DMaxD method on these datasets. In these figures, we provide the estimated

TABLE VI

SAD RESULTS ON UNIVERSITY OF PAVIA DATASET. THE MEAN AND STANDARD DEVIATION ARE REPORTED FOR EACH METHOD. THE BEST RESULTS ARE ILLUSTRATED IN BOLD.

Endm.	Spectral Angle Distance (SAD) ($\times 10^{-2}$)					
	VCA	DMaxD	SPICE	SCM	EndNet-VCA	EndNet-DMaxD
#1	51.02 \pm 8.9	7.50 \pm 0.0	57.98 \pm >9	2.93 \pm 0.0	2.31 \pm 1.1	2.38 \pm 0.6
#2	39.43 \pm >9	92.98 \pm 0.0	66.33 \pm >9	1.85 \pm 0.0	4.19 \pm 1.1	6.07 \pm 1.8
#3	28.85 \pm >9	>99 \pm 0.0	12.50 \pm 5.3	4.70 \pm 0.0	1.62 \pm 0.1	2.03 \pm 0.8
#4	42.47 \pm 4.6	30.60 \pm 0.0	44.45 \pm >9	11.67 \pm 0.0	10.11 \pm 1.2	8.57 \pm 1.7
#5	85.19 \pm >9	70.95 \pm 0.0	>99 \pm >9	7.69 \pm 0.0	5.73 \pm 0.6	7.04 \pm 0.8
#6	42.65 \pm 8.8	56.93 \pm 0.0	93.00 \pm >9	27.65 \pm 0.0	4.62 \pm 2.6	1.59 \pm 0.5
#7	53.04 \pm 3.7	53.06 \pm 0.0	94.72 \pm >9	5.29 \pm 0.0	55.80 \pm 0.3	13.40 \pm 1.9
Avg.	48.96 \pm >9	61.33 \pm 0.0	67.79 \pm >9	8.82 \pm 0.0	12.07 \pm 1.0	5.87 \pm 1.2

TABLE VII

SAD RESULTS ON UNIVERSITY OF PAVIA DATASET. THE MEAN AND STANDARD DEVIATION ARE REPORTED FOR EACH METHOD. THE BEST RESULTS ARE ILLUSTRATED IN BOLD.

Endm.	Spectral Angle Distance (SAD) ($\times 10^{-2}$)					
	VCA	DMaxD	SPICE	SCM	EndNet-VCA	EndNet-DMaxD
#1	17.04 \pm >9	12.71 \pm 0.0	>99 \pm >9	15.31 \pm 0.0	3.47 \pm 1.0	2.75 \pm 0.2
#2	45.73 \pm >9	12.21 \pm 0.0	>99 \pm >9	2.07 \pm 0.0	6.32 \pm 5.2	1.28 \pm 0.1
#3	25.90 \pm 1.8	26.12 \pm 0.0	>99 \pm >9	1.93 \pm 0.0	9.99 \pm 8.4	3.97 \pm 0.4
#4	42.09 \pm >9	34.12 \pm 0.0	>99 \pm >9	4.78 \pm 0.0	13.55 \pm >9	8.31 \pm 0.7
#5	60.43 \pm 9.7	24.13 \pm 0.0	88.03 \pm >9	29.92 \pm 0.0	23.48 \pm >9	2.72 \pm 0.7
#6	39.10 \pm 9.0	47.06 \pm 0.0	>99 \pm >9	21.03 \pm 0.0	13.69 \pm >9	11.78 \pm 1.0
#7	37.42 \pm 4.7	9.28 \pm 0.0	46.60 \pm >9	6.40 \pm 0.0	8.66 \pm 2.5	11.56 \pm 0.4
Avg.	38.25 \pm >9	23.67 \pm 0.0	>99 \pm >9	11.65 \pm 0.0	11.31 \pm 7.9	6.06 \pm 0.5

abundance maps, the ground truth (if it is available) and the absolute differences of the estimated abundances and the ground truth for each material (if it is available). In addition, the estimated endmember and ground truth signatures are illustrated for Urban, Samson and Jasper datasets in Fig. 7, 10 and 12. (Please look at project website for the qualitative results of other datasets.)

Lastly, note that for SCM method, the parameters are tuned to $\beta_1 = 10$, $\beta_2 = 10$ and $\rho = 0.01$ for these four datasets.

Urban: Quantitative and qualitative results on Urban dataset are summarized in Table I and in Fig. 8. From the results, our method achieves the best overall scores for both SAD and RMSE metrics compared to other methods. EndNet-DMaxD approximately introduces 4.2% and 1.2% improvements to the second best result. The second best result is obtained by DgS-NMF method that exploits spatial priors in the estimation. This is important since our method outperforms the methods that use spatial information about data, without exploiting any extra prior.

Fig. 8 visualizes the estimated abundance map for the dataset with EndNet-DMaxD method. To compare the estimation accuracy, absolute differences of the estimated abundance map and ground truth are provided for each material (i.e rows). From these results, we can clearly observe that the estimation error usually concentrates on the object boundaries. Despite the fact that our method might yield false estimates where high spectral mixtures have occurred, we must emphasize that the ground truth can still exhibit some noise since the determination of perfect abundance labels of these locations can be challenging as expected.

Samson: Results are shown in Table II and Fig. 9. Similarly, our methods obtain the best overall performances for both metrics, and RMSE results are prominently improved by our method. Approximately, 2% and 3% improvements are

introduced for SAD and RMSE metrics respectively. From Fig. 9, it can be observed that the absolute difference is quite small. Only, the water-ground intersection areas yield small estimation error where all three materials can contribute.

Jasper Ridge: Remark that soil (#3) and road (#4) are highly mixed materials in this scene. Therefore, we redefine λ_2 as 0.4 to increase the sparsity of the material signatures in our method. Table III shows the SAD and RMSE performances of the methods. From the results, our method introduces small improvements over DgS-NMF. However, it should not be discarded that even if the use of spatial priors provides huge advantages, our method still yields the best results for the highly mixed scenes. Fig. 11 illustrates the absolute error with the ground truth. Particularly, the error is intensified at the boundaries of water-ground as well as road-soil.

Lastly, an important observation for one of our methods is that the performances of EndNet-VCA drastically drop down on this dataset while EndNet-DMaxD obtains the state-of-the-art performance. Our explanation to this result is that DMaxD method is inclined to detect more uncorrelated spectral signatures from data compared to VCA (even if the estimates do not need to be true results), since it maximizes the distances

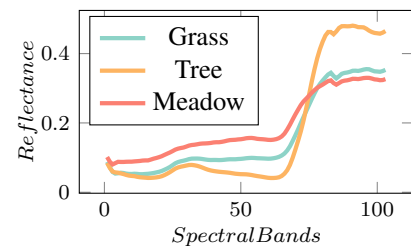


Fig. 15. Three highly correlated materials observed in University of Pavia dataset: Grass, Tree and Meadow. Even if Grass and Meadow are considered as one constituent material in the original dataset, they have two distinct spectral signatures as shown in the plot.

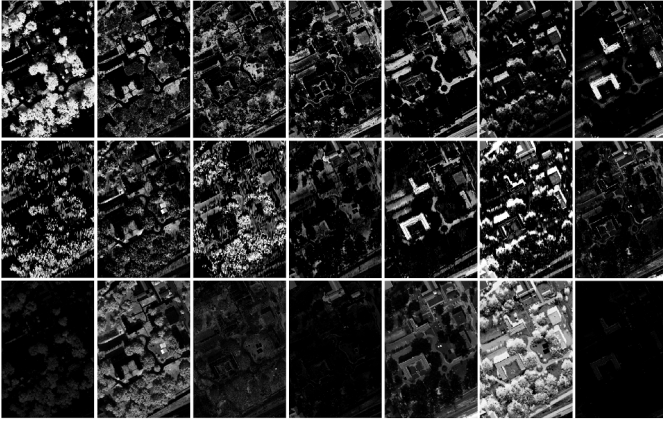


Fig. 16. Estimated abundance maps on University of Pavia dataset. Rows indicate methods: EndNet-DMaxD, SCM and SPICE, while each column corresponds to the abundance map of a single material: Asphalt-Bitumen (#1), Meadows (#2), Trees (#3), Metal Sheets (#4), Bare Soil (#5), Gravel-Bricks (#6) and Shadow (#7) respectively. We also visualize the abundance map of Grass material obtained by EndNet-DMaxD method as the last image.

of the estimated spectral signatures with one another. Also, VCA can ignore the materials that are numerically small in a scene. Thus, considering the methods like DMaxD for our method initialization can be more convenient.

Cuprite: Experimental results for this dataset are reported in Table IV and Fig. 13. From these results, it is clear that the methods using the unmixed pixel assumption such as VCA, DMaxD etc. obtain high performances. Therefore, we decreased the value of the sparsity term λ_2 to 0.001. Another important feature of the dataset is that it consists of quite correlated materials. For this reason, we also set p as 0.8 to improve the convergence of the parameters.

The experimental results show that our methods estimate the lowest SAD results compared to the baseline methods. Moreover, Fig. 13 visualizes the estimated abundance map for each material with EndNet-DMaxD method. Since this dataset has no ground truth for the true abundances, we can only make visual comparisons to analyze the consistency with other methods [72]. When we compare our results with [72], we can observe that the estimated abundance maps are consisted with the reported visual results.

Comparison of Abundance Map Estimation: The detailed experimental results for the abundance map estimation of SPU and EndNet-DMaxD are reported in Table V. For three datasets, SPU method introduces further improvements to the performances compared to EndNet-DMaxD abundance estimates. However, note that EndNet-DMaxD achieves similar or better performances compared to the baseline methods.

D. Experiments on Hyperspectral Classification Datasets

In this section, we analyze SAD and qualitative performances of the baseline methods on University of Pavia and Mississippi Gulfport datasets. Similarly, tests are repeated 20 times. Fig. 14 illustrates these datasets and their pixel-wise class labels. Note that no RMSE performance on abundance map estimates is reported on the contrary to [75], since class

labels are quite noisy and this information might not convey true performances.

Moreover, despite there is no endmember ground truth available for these datasets, we used the average spectras of the pixels for each material as the ground truth in SAD comparisons as proposed in [75], [76].

Table VI and VII show the SAD performances of the methods. Also, Fig. 16 and 17 visualize the qualitative abundance map performances for three methods: SPICE, SCM and EndNet-DMaxD (VCA, DMaxD and MVSA methods obtain insufficient abundance results). Remark that $l_{1|2}$ -NMF and DgS-NMF scores are not reported since neither their source codes nor previous performances are available on these datasets.

For University of Pavia dataset, the parameters are set to $\beta_1 = 10$, $\beta_2 = 10$ and $\rho = 0.01$ for SCM method. These values are slightly different from the recommended settings in [75], since these configurations yield better visual and quantitative results in our experiments. Similarly, for Mississippi Gulfport, these values are tuned to $\beta_1 = 10$, $\beta_2 = 5$ and $\rho = 0.01$. Lastly, the prune threshold value is increased to 10^{-5} for SPICE algorithm on Mississippi Gulfport dataset.

University of Pavia: Table VI and Fig. 16 show experimental results on this dataset. As mentioned, the scene contains 7 labeled classes after the associations of gravel-bricks and asphalt-bitumen materials. However, we empirically observed that the scene comprises another distinct material, 'Grass', which has completely different spectral reflectances from 'Meadow' and 'Tree'. These three materials are plotted in Fig. 15.

For this reason, we set the optimum endmember number in the scene as 8 just for our method and preserved the default value (i.e. 7) for the baseline methods (for these methods, they yield worse results when we increase the endmember number).

We redefine λ_2 and p as 0.01 and 0.8 respectively similar to Cuprite dataset, since the data contains quite correlated materials. Differently, we decreased mask noise to 10% due the noise level of data and again material spectral correlations. From SAD results, it is clear that our method obtains the best

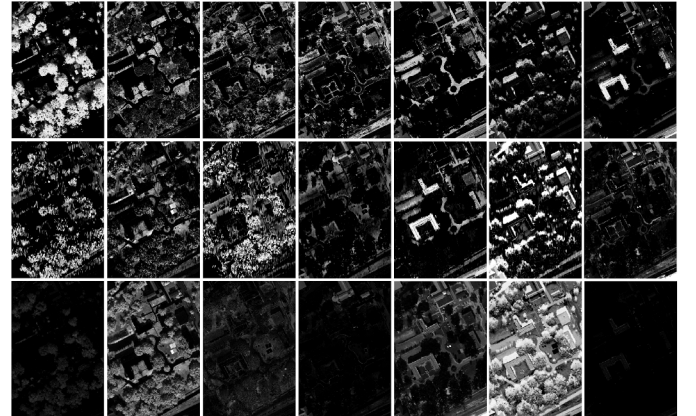


Fig. 17. Abundance maps for Mississippi Gulfport dataset. Similarly, the results of EndNet-DMaxD, SCM and SPICE are illustrated in different rows respectively. Trees (#1), Grass Pure (#2), Grass Ground (#3), Dirt & Sand (#4), Road (#5), Shadow (#6) and Building (#7) are identified in columns.

performance compared to the baselines and approximately 3% improvement is introduced over the second best result.

Of course, abundance map estimation is especially important for this dataset to distinguish the classes truly. Fig. 16 visualizes the abundance map estimations for three methods. It can be easily seen that our method, EndNet-DMaxD, outperforms other baseline methods and obtains meaningful abundance results for the materials. Particularly, considering 'Grass' material in hyperspectral unmixing provides critical improvements to the scene areas where 'Trees' are repeatedly miscategorized with 'Grass'/'Meadow' by the baseline methods.

Mississippi Gulfport: Quantitative and qualitative results for this dataset are reported in Table VII and Fig. 17. Similarly, λ_2 and p values are tuned as 0.1 and 0.8, and mask noise is set to 10%. Several materials (i.e. sidewalk, yellow curb, cloth panels and water) are not considered in the computation, since their samples are too scarce in the scene.

In Table VII, our method yields the highest overall SAD score over ground truth materials and the quality of abundance map estimates in Fig. 17 are significantly better compared to the baselines. Particularly, for 'Tree', 'Building' and 'Shadow', misprediction rates are quite high for the baseline methods, whereas our method obtains nearly optimum results for these materials in the scene.

IV. CONCLUSION

In this paper, we propose a novel method, EndNet, for endmember extraction and hyperspectral unmixing. For this purpose, we improve and restructure the conventional autoencoder neural network by introducing additional layers and a novel loss function. These modifications enable us to conserve the common features of hyperspectral unmixing such as nonlinearity, sparsity, some of the physical constraints etc. that are essential to solve this problem. Also, backpropagation with a stochastic-gradient based solver is used to optimize the problem and it scales the method for large-scale data, instead of complex derivations/inferences in literature.

Moreover, we adapt SPU algorithm to further improve the estimation of abundance maps from a scene with the estimated endmembers, even if the estimates of hidden abstracts yield compatible results. This adaptation is achieved by replacing the standard l_2 norm kernel with SAD kernel that is more convenient for our model as explained.

From the experimental results, it is clearly observed that our method makes significant performance improvements to hyperspectral unmixing domain and achieves the state-of-the-art performances on well-known hyperspectral datasets. In addition, we particularly select the method DgS-NMF as a baseline technique in the experiments to show that our method outperforms this type of methods even if they use the spatial priors of a scene in the extraction.

Finally, we should emphasize that our method is the first successful end-to-end learning attempt based on a neural network that attains superior performances all in an unsupervised manner for hyperspectral unmixing problem. That's why, we strongly believe that the findings of our paper will provide a

basis to further studies on neural network techniques in this domain.

ACKNOWLEDGMENT

The authors would like to thank Engin Tola and Ufuk Sakarya for proofreading this manuscript.

REFERENCES

- [1] J. M. Bioucas-Dias, A. Plaza, N. Dobigeon, M. Parente, Q. Du, P. Gader, and J. Chanussot, "Hyperspectral unmixing overview: Geometrical, statistical, and sparse regression-based approaches," *IEEE JSTARS*, pp. 354–379, 2012.
- [2] B. Hapke, "Bidirectional reflectance spectroscopy: 1. theory," *Journal of Geophysical Research: Solid Earth*, pp. 3039–3054, 1981.
- [3] J. M. Nascimento and J. M. Dias, "Vertex component analysis: A fast algorithm to unmix hyperspectral data," *IEEE TGRS*, pp. 898–910, 2005.
- [4] J. W. Boardman, "Geometric mixture analysis of imaging spectrometry data," in *IGARSS*. IEEE, 1994, pp. 2369–2371.
- [5] J. C. Harsanyi and C.-I. Chang, "Hyperspectral image classification and dimensionality reduction: An orthogonal subspace projection approach," *IEEE TGRS*, pp. 779–785, 1994.
- [6] M. E. Winter, "N-findr: An algorithm for fast autonomous spectral end-member determination in hyperspectral data," in *SPIE*, 1999, pp. 266–275.
- [7] R. Heylen, D. Burazerovic, and P. Scheunders, "Non-linear spectral unmixing by geodesic simplex volume maximization," *IEEE J-STSP*, pp. 534–542, 2011.
- [8] M.-D. Iordache, J. M. Bioucas-Dias, and A. Plaza, "Sparse unmixing of hyperspectral data," *IEEE TGRS*, pp. 2014–2039, 2011.
- [9] R. B. Singer and T. B. McCord, "Mars-large scale mixing of bright and dark surface materials and implications for analysis of spectral reflectance," in *Lunar and Planetary Science Conference Proceedings*, 1979, pp. 1835–1848.
- [10] A. Ifarraguerri and C.-I. Chang, "Multispectral and hyperspectral image analysis with convex cones," *IEEE TGRS*, pp. 756–770, 1999.
- [11] F.-Y. Wang, C.-Y. Chi, T.-H. Chan, and Y. Wang, "Nonnegative least-correlated component analysis for separation of dependent sources by volume maximization," *IEEE PAMI*, pp. 875–888, 2010.
- [12] V. F. Haertel and Y. E. Shimabukuro, "Spectral linear mixing model in low spatial resolution image data," *IEEE TGRS*, pp. 2555–2562, 2005.
- [13] L. Miao and H. Qi, "Endmember extraction from highly mixed data using minimum volume constrained nonnegative matrix factorization," *IEEE TGRS*, pp. 765–777, 2007.
- [14] J. Li and J. M. Bioucas-Dias, "Minimum volume simplex analysis: A fast algorithm to unmix hyperspectral data," in *IGARSS*. IEEE, 2008.
- [15] N. Dobigeon, S. Moussaoui, M. Coulon, J.-Y. Tourneret, and A. O. Hero, "Joint bayesian endmember extraction and linear unmixing for hyperspectral imagery," *IEEE Transactions on Signal Processing*, pp. 4355–4368.
- [16] M.-D. Iordache, J. M. Bioucas-Dias, and A. Plaza, "Collaborative sparse regression for hyperspectral unmixing," *IEEE TGRS*, pp. 341–354, 2014.
- [17] B. Somers, K. Cools, S. Delalieux, J. Stuckens, D. Van der Zande, W. W. Verstraeten, and P. Coppin, "Nonlinear hyperspectral mixture analysis for tree cover estimates in orchards," *Remote Sensing of Environment*, vol. 113, no. 6, pp. 1183–1193, 2009.
- [18] N. Keshava and J. F. Mustard, "Spectral unmixing," *IEEE Signal Processing Magazine*, pp. 44–57, 2002.
- [19] S. T. Roweis and L. K. Saul, "Nonlinear dimensionality reduction by locally linear embedding," *Science*, pp. 2323–2326, 2000.
- [20] C. M. Bachmann, T. L. Ainsworth, and R. A. Fusina, "Improved manifold coordinate representations of large-scale hyperspectral scenes," *IEEE TGRS*, pp. 2786–2803, 2006.
- [21] G. Zhao, C. Zhao, and X. Jia, "Multilayer unmixing for hyperspectral imagery with fast kernel archetypal analysis," *IEEE GRSL*, pp. 1532–1536.
- [22] J. Broadwater and A. Banerjee, "A comparison of kernel functions for intimate mixture models," in *IEEE WHISPERS*. IEEE, 2009, pp. 1–4.
- [23] J. Chen, C. Richard, and P. Honeine, "Nonlinear unmixing of hyperspectral data based on a linear-mixture/nonlinear-fluctuation model," *IEEE Transactions on Signal Processing*, pp. 480–492, 2013.
- [24] C. Févotte and N. Dobigeon, "Nonlinear hyperspectral unmixing with robust nonnegative matrix factorization," *IEEE Transactions on Image Processing*, pp. 4810–4819, 2015.

- [25] R. Close, P. Gader, J. Wilson, and A. Zare, "Using physics-based macroscopic and microscopic mixture models for hyperspectral pixel unmixing," in *SPIE*, 2012, p. 83901L.
- [26] Y. Altmann, N. Dobigeon, and J.-Y. Tourneret, "Bilinear models for nonlinear unmixing of hyperspectral images," in *IEEE WHISPERS*. IEEE, 2011, pp. 1–4.
- [27] R. Heylen, P. Scheunders, A. Rangarajan, and P. Gader, "Nonlinear unmixing by using different metrics in a linear unmixing chain," *IEEE JSTARS*, pp. 2655–2664, 2015.
- [28] F. Kizel, M. Shoshany, N. S. Netanyahu, G. Even-Tzur, and J. A. Benediktsson, "A stepwise analytical projected gradient descent search for hyperspectral unmixing and its code vectorization," *IEEE TGRS*, 2017.
- [29] J. Plaza, A. Plaza, R. Perez, and P. Martinez, "On the use of small training sets for neural network-based characterization of mixed pixels in remotely sensed hyperspectral images," *Pattern Recognition*, pp. 3032–3045, 2009.
- [30] K. J. Guilfoyle, M. L. Althouse, and C.-I. Chang, "A quantitative and comparative analysis of linear and nonlinear spectral mixture models using radial basis function neural networks," *IEEE TGRS*, pp. 2314–2318, 2001.
- [31] J. Plaza, A. Plaza, R. Pérez, and P. Martinez, "Joint linear/nonlinear spectral unmixing of hyperspectral image data," in *IGARSS*. IEEE, 2007, pp. 4037–4040.
- [32] B. Ayerdi and M. Grana, "Hyperspectral image nonlinear unmixing and reconstruction by elm regression ensemble," *Neurocomputing*, pp. 299–309.
- [33] B. Pan, Z. Shi, and X. Xu, "R-vcanet: A new deep-learning-based hyperspectral image classification method," *IEEE JSTAR*, pp. 1975–1986.
- [34] R. Guo, W. Wang, and H. Qi, "Hyperspectral image unmixing using autoencoder cascade," in *IEEE WHISPERS*, 2015, pp. 1–4.
- [35] E. Batı, A. Caliskan, A. Koz, and A. A. Alatan, "Hyperspectral anomaly detection method based on auto-encoder," in *SPIE*, 2015, pp. 96430N–1.
- [36] F. Palsson, J. Sigurdsson, J. Sveinsson, and M. Ulfarsson, "Neural network hyperspectral unmixing with spectral information divergence objective," *IGARSS*, 2017.
- [37] V. Nair and G. E. Hinton, "Rectified linear units improve restricted boltzmann machines," in *ICML*, 2010, pp. 807–814.
- [38] S. Ioffe and C. Szegedy, "Batch normalization: Accelerating deep network training by reducing internal covariate shift," in *ICML*, 2015, pp. 448–456.
- [39] N. Srivastava, G. E. Hinton, A. Krizhevsky, I. Sutskever, and R. Salakhutdinov, "Dropout: a simple way to prevent neural networks from overfitting," *JMLR*, no. 1, pp. 1929–1958, 2014.
- [40] S. Wager, S. Wang, and P. S. Liang, "Dropout training as adaptive regularization," in *NIPS*, 2013, pp. 351–359.
- [41] P. Vincent, H. Larochelle, I. Lajoie, Y. Bengio, and P.-A. Manzagol, "Stacked denoising autoencoders: Learning useful representations in a deep network with a local denoising criterion," *Journal of Machine Learning Research*, vol. 11, no. Dec, pp. 3371–3408, 2010.
- [42] Y. Bengio, A. Courville, and P. Vincent, "Representation learning: A review and new perspectives," *IEEE PAMI*, pp. 1798–1828, 2013.
- [43] Y. LeCun, Y. Bengio, and G. Hinton, "Deep learning," *Nature*, pp. 436–444, 2015.
- [44] S. Rifai, P. Vincent, X. Muller, X. Glorot, and Y. Bengio, "Contractive auto-encoders: Explicit invariance during feature extraction," in *ICML*, 2011, pp. 833–840.
- [45] A. Rasmus, M. Berglund, M. Honkala, H. Valpola, and T. Raiko, "Semi-supervised learning with ladder networks," in *NIPS*, 2015, pp. 3546–3554.
- [46] S. Holzwarth, A. Muller, M. Habermeyer, R. Richter, A. Hausold, S. Thiemann, and P. Strobl, "Hysens-dais 7915/rosis imaging spectrometers at dlr," in *Proceedings of the 3rd EARSeL Workshop on Imaging Spectroscopy*, 2003, pp. 3–14.
- [47] K. He, X. Zhang, S. Ren, and J. Sun, "Delving deep into rectifiers: Surpassing human-level performance on imagenet classification," in *ICCV*, 2015, pp. 1026–1034.
- [48] R. Memisevic and D. Krueger, "Zero-bias autoencoders and the benefits of co-adapting features," *Stat*, p. 13, 2014.
- [49] D.-A. Clevert, T. Unterthiner, and S. Hochreiter, "Fast and accurate deep network learning by exponential linear units (elus)," *arXiv preprint arXiv:1511.07289*, 2015.
- [50] B. Xu, N. Wang, T. Chen, and M. Li, "Empirical evaluation of rectified activations in convolutional network," *arXiv preprint arXiv:1505.00853*, 2015.
- [51] A. Krizhevsky, I. Sutskever, and G. E. Hinton, "Imagenet classification with deep convolutional neural networks," in *NIPS*, 2012, pp. 1097–1105.
- [52] A. Makhzani and B. Frey, "K-sparse autoencoders," *arXiv preprint arXiv:1312.5663*, 2013.
- [53] Y. LeCun, B. Boser, J. S. Denker, D. Henderson, R. E. Howard, W. Hubbard, and L. D. Jackel, "Backpropagation applied to handwritten zip code recognition," *Neural computation*, pp. 541–551, 1989.
- [54] L. Chunjie, Y. Qiang et al., "Cosine normalization: Using cosine similarity instead of dot product in neural networks," *arXiv preprint arXiv:1702.05870*, 2017.
- [55] P. E. Dennison, K. Q. Halligan, and D. A. Roberts, "A comparison of error metrics and constraints for multiple endmember spectral mixture analysis and spectral angle mapper," *Remote Sensing of Environment*, pp. 359–367, 2004.
- [56] G. Camps-Valls, "Kernel spectral angle mapper," *Electronics Letters*, pp. 1218–1220, 2016.
- [57] G. Camps-Valls, L. Gomez-Chova, J. Muñoz-Marí, J. Vila-Francés, and J. Calpe-Maravilla, "Composite kernels for hyperspectral image classification," *IEEE GRSL*, pp. 93–97, 2006.
- [58] M. Fauvel, J. Chanussot, and J. A. Benediktsson, "Evaluation of kernels for multiclass classification of hyperspectral remote sensing data," in *ICASSP*. IEEE, 2006.
- [59] H. Li and L. Zhang, "A hybrid automatic endmember extraction algorithm based on a local window," *IEEE GRSL*, pp. 4223–4238.
- [60] X. Liu and C. Yang, "A kernel spectral angle mapper algorithm for remote sensing image classification," in *Image and Signal Processing*. IEEE, 2013, pp. 814–818.
- [61] F. Tsai and W. Philpot, "Derivative analysis of hyperspectral data," *Remote Sensing of Environment*, pp. 41–51, 1998.
- [62] Z. B. Rabah, I. R. Farah, G. Mercier, and B. Solaiman, "A new method to change illumination effect reduction based on spectral angle constraint for hyperspectral image unmixing," *IEEE GRSL*, pp. 1110–1114, 2011.
- [63] J. R. Hershey and P. A. Olsen, "Approximating the kullback leibler divergence between gaussian mixture models," in *ICASSP*. IEEE, 2007, pp. IV–317.
- [64] L. v. d. Maaten and G. Hinton, "Visualizing data using t-sne," *JMLR*, pp. 2579–2605, 2008.
- [65] K. Kavukcuoglu, M. Ranzato, and Y. LeCun, "Fast inference in sparse coding algorithms with applications to object recognition," *arXiv preprint arXiv:1010.3467*, 2010.
- [66] D. Kingma and J. Ba, "Adam: A method for stochastic optimization," *arXiv preprint arXiv:1412.6980*, 2014.
- [67] D. Ulyanov, A. Vedaldi, and V. Lempitsky, "Instance normalization: The missing ingredient for fast stylization," *arXiv:1607.08022*, 2016.
- [68] R. Heylen, D. Burazerovic, and P. Scheunders, "Fully constrained least squares spectral unmixing by simplex projection," *IEEE TGRS*, pp. 4112–4122, 2011.
- [69] Y. Qian, S. Jia, J. Zhou, and A. Robles-Kelly, "Hyperspectral unmixing via $L_{\{1/2\}}$ sparsity-constrained nonnegative matrix factorization," *IEEE TGRS*, pp. 4282–4297, 2011.
- [70] F. Zhu, Y. Wang, B. Fan, S. Xiang, G. Meng, and C. Pan, "Spectral unmixing via data-guided sparsity," *IEEE TIP*, pp. 5412–5427, 2014.
- [71] F. Zhu, Y. Wang, S. Xiang, B. Fan, and C. Pan, "Structured sparse method for hyperspectral unmixing," *ISPRS Journal of Photogrammetry and Remote Sensing*, pp. 101–118, 2014.
- [72] F. A. Kruse et al., "Comparison of aviris and hyperion for hyperspectral mineral mapping," in *11th JPL Airborne Geoscience Workshop*, 2002.
- [73] P. Gader, A. Zare, R. Close, J. Aitken, and G. Tuell, "Muufi gulfport hyperspectral and lidar airborne data set," *Univ. Florida, Gainesville, FL, USA, Tech. Rep. REP-2013-570*, 2013.
- [74] A. Zare and P. Gader, "Sparsity promoting iterated constrained end-member detection in hyperspectral imagery," *IEEE GRSL*, pp. 446–450, 2007.
- [75] Y. Zhou, A. Rangarajan, and P. D. Gader, "A spatial compositional model for linear unmixing and endmember uncertainty estimation," *IEEE TIP*, pp. 5987–6002, 2016.
- [76] A. Zare, P. Gader, O. Bchir, and H. Frigui, "Piecewise convex multiple-model endmember detection and spectral unmixing," *IEEE TGRS*, pp. 2853–2862, 2013.